Journal of Alloys and Compounds 1003 (2024) 175613

Contents lists available at ScienceDirect

Journal of Alloys and Compounds

journal homepage: www.elsevier.com/locate/jalcom

The influence of microstructure on the oxidation behavior of a TaTiCr refractory complex concentrated alloy

Noah J. Welch [a,b,c,d], Todd M. Butler [e], Maria J. Quintana [a,b,c], Peter C. Collins [a,b,c,*]

[a] Department of Materials Science and Engineering, Iowa State University, Ames, IA 50011, USA
[b] Center for Advanced Non-Ferrous Structural Alloys (CANFSA), USA
[c] Ames Laboratory, Iowa State University, Ames, IA 50011, USA
[d] Department of Energy's Kansas City National Security Campus Managed by Honeywell FM&T, Kansas City, MO 64147, USA
[e] Air Force Research Laboratory, Materials and Manufacturing Directorate, Wright-Patterson Air Force Base, OH 45433, USA

ARTICLE INFO

Keywords:
Microstructure
Oxidation
Complex oxide
TaTiCr
Refractory alloy
RCCA

ABSTRACT

This work explores the effect of microstructure on the oxidation behavior of an equiatomic TaTiCr RCCA after 24 h of exposure at 800°C, 1000°C, 1200°C, and 1400°C. Two microstructural conditions, both containing a *bcc* matrix with C15 Laves precipitates, with one condition having coarser precipitates (~10.9 μm diameter) and one condition having finer precipitates (~2.9 μm diameter) were studied. At all oxidation temperatures except 800°C, the finer-scale (TaTiCr-F) condition experienced more rapid oxidation kinetics, higher mass gains, and thicker oxide scales and internal reaction zones. However, at 800°C, the microstructure containing coarser precipitates (TaTiCr-C) formed a thicker oxide scale. Continuous, protective Cr_2O_3 layers were only observed in the coarse precipitate condition and correlations between Cr_2O_3 layer thickness, subsequent formation of complex refractory oxides, and the initial Laves precipitate size are described. It is proposed that the formation of continuous Cr_2O_3 is highly dependent on the size and distribution of the Cr-rich Laves phase and only mildly dependent on phase fraction. Oxidation mechanisms for each condition are discussed relative to the initial microstructures, observed oxide species, and related alloy systems.

1. Introduction

Development of high-temperature aerospace alloys that can withstand temperatures above 1000°C is of great interest for many advancing and emerging technologies. Potential applications such as advanced heat exchangers, thrusters and nozzles, and other atmosphere-exposed advanced aerospace components. These applications push beyond the operating limits of current state-of-the-art Ni-base superalloys. Conventional refractory alloys are capable of maintaining suitable mechanical strength at these temperatures. However, such alloys inherently form harmful, deleterious oxides (e.g., Ta_2O_5, Nb_2O_5) in the presence of oxygen at high temperatures, leading to catastrophic oxidation of metallic parts [1–9]. This drastically limits their use case and generally requires the use of complex coatings which add to complexity and cost [10].

Refractory complex concentrated alloys (RCCAs) and/or refractory high entropy alloys (RHEAs) have shown immense promise for these higher temperature regimes, albeit in limited-lifetime use cases, since these alloys can exhibit suitable mechanical properties and have shown anomalous oxidation resistance at temperatures above 1000°C [1,11–24]. While the retained high temperature strength is not surprising, the enhancement of oxidation resistance is unexpected. For the latter, RCCAs tend to form thermodynamically favorable complex oxides (e.g., $CrTaO_4$) due to their compositional complexity, which serve to neutralize the formation of harmful simple oxides. Particular complex refractory oxides (e.g., $CrNbO_4$, $CrTaO_4$) have been reported to offer reasonable oxidation resistance, especially when formed in tandem with other protective oxides such as Cr_2O_3 [15–17,25–30].

The TaTiCr alloy system has been of specific interest in recent studies due to its unique combination of mechanical properties and oxidation resistance [26,27]. The equiatomic TaTiCr alloy has shown great oxidation resistance at 1200°C and moderate resistance at 1400°C [27]. This alloy is similar to other oxidation resistant RCCAs, such as TaMoCrTiAl, studied in-depth by Schellert et al. [16,28–30]. Of note, the TaTiCr alloy forms a Ti-rich disordered bcc matrix with Cr-rich C15 Laves precipitates. These precipitates have been reported to act as Cr

* Corresponding author at: Department of Materials Science and Engineering, Iowa State University, Ames, IA 50011, USA.
E-mail address: pcollins@iastate.edu (P.C. Collins).

https://doi.org/10.1016/j.jallcom.2024.175613
Received 2 May 2024; Received in revised form 29 June 2024; Accepted 16 July 2024
Available online 16 July 2024

reservoirs during oxidation, readily supplying the surface of the specimen with Cr cations to form protective Cr_2O_3 layers and subsequent complex oxides such as $(Cr,Ta,Ti)O_2$ [27]. Schellert et al. [29] also recently reported that the substitution of Ti^{4+} on Cr^{3+} sites in $(Cr,TaTi)O_2$ may contribute to the inherent protectiveness of the oxide by reducing the concentration of oxygen vacancies, thereby limiting diffusion through the scale.

The oxidation behavior of equiatomic TaTiCr has been reported to change significantly with temperature, exhibiting an order of magnitude increase in mass gain after 24 h of exposure from 800°C (1.8 mg/cm^2) to 1400°C (26.0 mg/cm^2) [27]. However, the oxidation behavior of this alloy – along with an overwhelming majority of other RCCAs – has only been probed in the as-cast or hot-isostatically pressed (HIP) condition, and therefore, a single microstructural state [31]. The microstructures of most engineering alloys are carefully tailored to achieve desirable properties to satisfy demands of specific applications, and the same will likely be true for RCCAs. While the influence of grain size and precipitate size has been studied in conventional alloys for decades [32–36], this effect has not been readily explored in RCCAs. It is unknown what role microstructure plays on the resulting oxidation mechanisms in concentrated alloys.

When considering classic protective-oxide-forming alloys (e.g., Cr_2O_3, Al_2O_3), a refined grain structure generally corresponds to improved oxidation performance due to increased diffusion pathways for protective cations to diffuse to the surface, expediting the initial, transient stages of oxidation [36–38]. Likewise, alloys containing finer, well-dispersed precipitates that supply cations via the reservoir effect have been reported to improve oxidation resistance by enhancing scale continuity [39]. These mechanisms have not been explored in RCCAs. For 3d-transition high entropy alloys, Butler et al. [40] conducted a study on the effect of annealing on oxidation behaviors in *bcc/fcc* + B2 AlCoCrFeNi alloys and observed that annealing stabilized the microstructure during testing and caused the oxidation kinetics to adhere to parabolic behavior for a greater duration of testing. However, a slightly larger specific mass gain was reported in the annealed specimens. Results from a similar study conducted by Pavel, et al. [41] investigated precipitate size effects in a $Ni_{45}Co_{17}Cr_{14}Fe_{12}Al_7Ti_5$ MPEA and showed that smaller, highly concentrated precipitates resulted in less overall specific mass gain in both isothermal and cyclic oxidation tests. Additionally, an oxidation study on grain size effects of $NbCr_2$ Laves-containing alloys by Zheng, et al. showed that refined-grained conditions initially oxidize at a faster rate but slow with increased exposure time when compared to coarse-grained conditions at temperatures of 950°C to 1200°C [42].

This study elucidates the influence of precipitate size on the oxidation behaviors of a TaTiCr RCCA, building on previous work on the oxidation behavior of TaTiCr at 800, 1000, 1200, and 1400°C [27]. The experimental results are compared to related alloys and correlations between microstructure feature statistics and oxidation behavior are proposed. New fundamental insights provide perspective into the true oxidation behavior of these concentrated alloy systems by considering microstructure.

2. Materials and methods

TaTiCr alloy buttons with fine precipitates (identified as TaTiCr-F) and cigars with coarse precipitates (identified as TaTiCr-C) were vacuum-arc melted from high-purity powders (99.995 %). Both types of melts (button and cigar) were prepared on a water-cooled copper hearth and flipped several times to promote homogeneity. To ensure chemical uniformity in the specimens after casting, each button was wrapped in Ta foil and homogenized by hot isostatic pressing (HIP) for 3 hours at 1400°C and 207 MPa, under a high-purity Ar atmosphere. Heating/cooling rates were ~15 °C/min. After HIP, bulk alloy compositions were measured using inductively coupled plasma – optical emissions spectroscopy (ICP-OES) per ASTM E 2371–13. Carbon content was measured using combustion infrared absorption per ASTM E 1409–13 and oxygen and nitrogen content was measured using inert gas fusion per ASTM 1941–16. All elements were rounded per ASTM E29 and are reported in Table 1.

Oxidation tests were conducted using a Netzch Jupiter 449 F3 simultaneous thermal analyzer (STA). Due to constraints associated with the size of the crucible, cube specimens with 3 mm edge lengths were sectioned from the HIP ingots using a precision diamond saw. In preparation for oxidation testing, specimens were placed in alumina crucibles on top of a layer of calcined alumina powder to avoid reaction with the crucible for the duration of the tests. Oxidation tests were performed at 800, 1000, 1200, and 1400°C with a heating rate of 30 °C/min. Specimens were subjected to a continuous flow of bottled air atmosphere at 80 ml/min with a 10 ml/min N_2 balance.[1] Specimen mass was continuously recorded during oxidation tests to obtain specific mass change with respect to initial surface area (mg/cm^2). Specimens were subsequently hot mounted in conductive phenolic resin and prepared using conventional metallographic techniques. Final polishing was done using a vibratory polisher and 0.04 μm colloidal silica solution for 18 hours. After mounting, specimens were cross-sectioned in half to image the center of the samples.

Microstructural analysis of the pre- and post-oxidized specimens was conducted using a combination of scanning electron microscopy (SEM) and energy dispersive X-ray spectroscopy (EDS).[2] Samples were imaged using an FEI Teneo LoVac SEM equipped with both secondary and backscattered electron detectors, as well as, an Oxford X-max EDS detector. Throughout this paper, all compositions are given in at%. All SEM imaging was conducted with an accelerating voltage of 15 keV and a beam current of 0.8 nA. Statistical analysis of the microstructures was performed using MIPAR™ image analysis software. Oxide scale continuity was performed by measuring the area fraction of the observed scale cross-section from the theoretical "fully dense" scale region created using the filled outline of the segmented oxide scale layer in MIPAR.

X-ray diffraction (XRD) spectra were collected from the HIP specimens. XRD scans were conducted using a Rigaku SmartLab diffractometer in parallel beam mode with Cu-Kα1 radiation ($\lambda = 1.5406$ Å) and a 2θ range of 20–80°. Post-processing of XRD data was conducted using Rigaku PDXL2 and CrystalDiffract™ software.

3. Results and discussion

3.1. Microstructures and phase compositions

The two microstructural conditions in this work resulted from using different arc-melt ingot shapes, where a smaller, cigar-shaped ingot resulted in the microstructure with coarser Laves precipitates (TaTiCr-C) seen in Fig. 1(a) and a larger, button-shaped ingot resulted in the microstructure seen in Fig. 1(b), containing much finer Laves precipitates (TaTiCr-F). After HIP, XRD analysis revealed that both alloys displayed prominent bcc and C15 Laves peaks (Fig. 1(c)). EDS analysis corroborated the XRD results, resulting in expected compositions for both the Laves and bcc phase (Table 1).

Morphologically speaking, the coarse Laves precipitates have more faceted edges (Fig. 1(a)) while the finer precipitates are more rounded in character (Fig. 1(b)). In general, there is little directionality to the

[1] The 80 ml/min flow in the STA was determined by measuring specific mass change from static air box furnace tests and adjusting flow as necessary to match the static air results.

[2] The reader may wonder whether there are other methods of measuring phase fractions and distributions. The use of EDS is important, as other techniques–including XRD or EBSD analysis–rely upon differences in the crystal structure and/or lattice parameter differences. The observed complex oxides have an identical crystal structure and very similar lattice parameters, requiring the use of chemical information to distinguish individual species.

Table 1
Alloy compositions (measured using ICP-OES, etc.), phase compositions (measured using SEM-EDS), and microstructural information for the TaTiCr-C and TaTiCr-F alloys.

Alloy	Phase	Composition (at%)						F_{Laves}	Avg. particle diameter (μm)	Avg. interparticle spacing (μm)
		Ta	Ti	Cr	C	O	N			
TaTiCr-C	Alloy	33.213	33.930	32.492	<0.031	0.327	0.007	44.5 ± 1.7	10.9 ± 2.3	4.3 ± 1.4
	bcc	32.3	56.0	11.7	-	-	-			
	Laves	28.8	13.8	57.4	-	-	-			
TaTiCr-F	Alloy	31.090	34.339	34.400	<0.040	0.120	0.001	37.9 ± 2.5	2.3 ± 1.2	2.0 ± 0.8
	bcc	35.9	50.3	13.8	-	-	-			
	Laves	29.7	13.5	56.8	-	-	-			

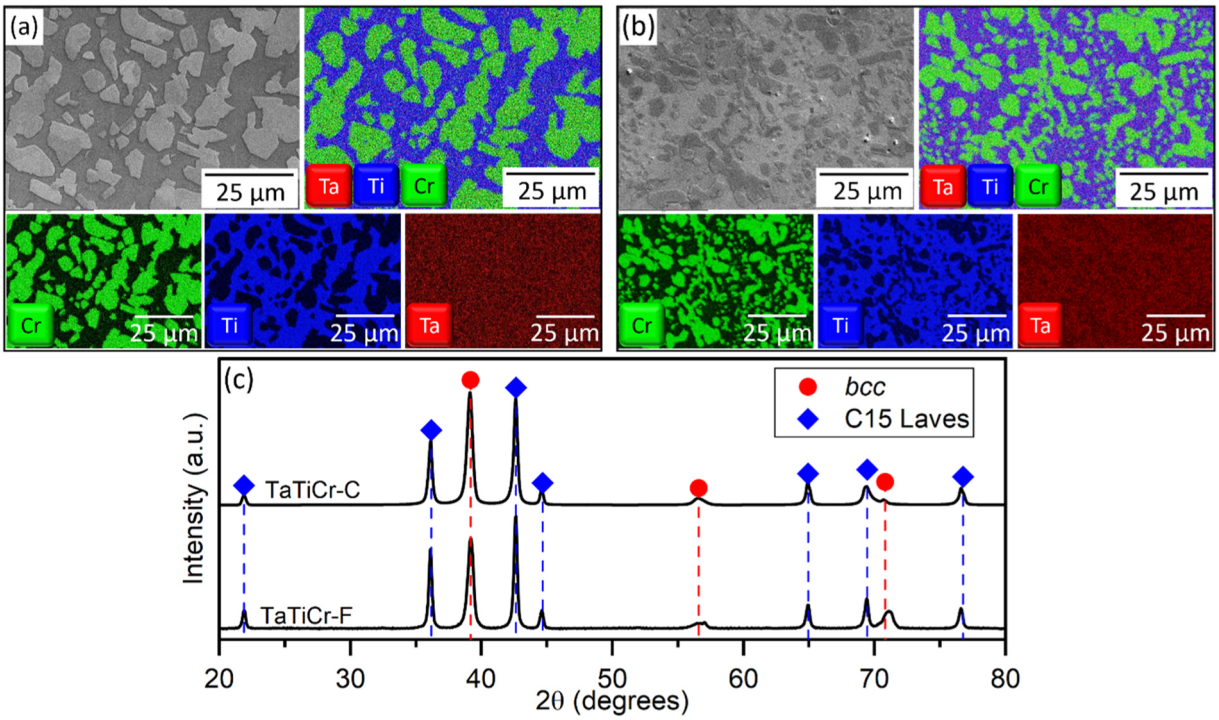

Fig. 1. Composite EDS maps of (a) TaTiCr-C alloy, with coarse Laves precipitates, (b) TaTiCr-F alloy, with fine Laves precipitates, and (c) XRD spectra for the two conditions captured after HIP process, displaying prominent bcc and C15 Laves peaks.

precipitates, and the average aspect ratio is near unity for both compositions. The volume of Laves precipitates was slightly higher in the coarse condition, as seen in Table 1. Additionally, the average diameter of coarse precipitates was >4x as large as the fine precipitates, and the interparticle spacing (measured edge-to-edge) was approximately twice as large (Table 1). Both microstructural conditions show features consistent with twin boundaries within the Laves phase, either caused by annealing twin effects or transformation twinning from the high-temperature C14 phase during cooling.

3.2. Oxidation kinetics of TaTiCr-C and TaTiCr-F

Fig. 2 shows specific mass change versus time for the TaTiCr-C condition (solid lines) and the TaTiCr-F condition (dashed lines) after oxidation testing for 24 h from 800°C to 1400°C. The rate of oxidation increases with temperature, and at all temperatures except 800°C, the TaTiCr-C condition displayed slower oxidation rates. The mass change curves were fitted using a general growth rate law:

$$\Delta m = kt^n \quad (1)$$

where Δm is the specific mass change with respect to initial surface area (mg/cm^2), k is the rate constant, t is the oxidation time, and n is the time exponent. Linear oxidation kinetics ($n = 1$) are generally considered to

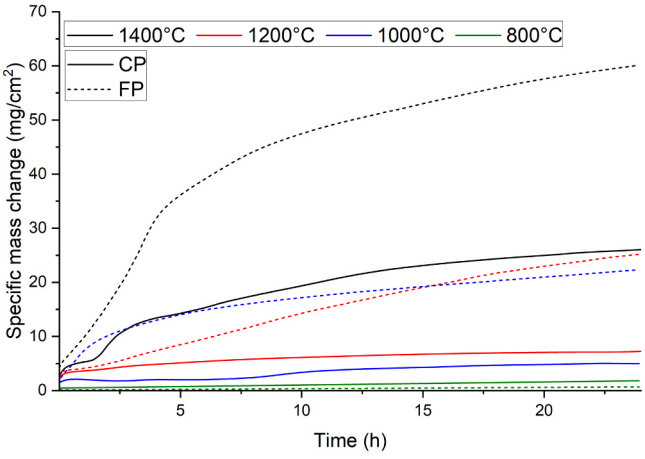

Fig. 2. Thermogravimetric data for the TaTiCr-C and TaTiCr-F alloys, tested for 24 h at 800°C, 1000°C, 1200°C, and 1400°C in simulated air.

be rate-limited by interfacial reactions, whereas parabolic oxidation kinetics ($n = 0.5$) are more preferred and controlled by anion and/or cation diffusion. Intermediate exponents between 1 and 0.5 are indicative of mixed-mode behavior, with both interfacial and diffusion-controlled effects. Kinetics where $n < 0.5$ usually indicate diffusion-controlled reactions combined with volatilization and mass loss effects.

The kinetic data reported in Table 2 shows a difference in time exponents between the two microstructural conditions (except for the 800°C test), indicating distinct variation in the oxidation mechanisms. At 800°C, both conditions displayed linear oxidation behavior (n = 1), but the TaTiCr-F alloy exhibited a smaller rate constant (0.02 vs. 0.06 mg/cm^2 h). For all other testing temperatures, the TaTiCr-F alloy experienced significantly larger mass gain during high temperature exposures. At 1000°C, the TaTiCr-C alloy exhibited a single, near-linear (n = 0.95) regime for the entire duration of the test, while TaTiCr-F displayed a mixed-mode regime (n = 0.74) for the first hour, which then transitioned into a parabolic regime (n = 0.48) for the remainder of the test (Table 2). At 1200°C, TaTiCr-C showed a single, sub-parabolic (n = 0.34) kinetic regime for the entire test, while TaTiCr-F exhibited a mixed-mode regime for the duration of the test (n = 0.83) (Table 2). At 1400°C, both TaTiCr-C and TaTiCr-F displayed two kinetic regimes. TaTiCr-C displayed a sub-parabolic regime (n = 0.37) from 0 to 2 h and a second sub-parabolic regime (n = 0.42) from 2 to 24 h, while TaTiCr-F showed a linear (n = 1.05) regime from 0 to 3 h, followed by a parabolic (n = 0.48) regime from 3 to 24 h (Table 2). The mechanisms responsible for the kinetic changes between microstructural conditions will be discussed in Section 3.3.

3.3. Post-oxidation microstructure of TaTiCr-C and TaTiCr-F conditions

Representative cross sections of the oxide scales and internal reaction zones (IRZ) after 24 hours of exposure are shown in Fig. 3. Significant differences in oxide scale and IRZ morphologies were observed between the coarse and fine microstructural conditions. Oxidation behaviors from 800°C-1400°C for the TaTiCr-C condition have been reported elsewhere [27], but are briefly highlighted here for comparison with the TaTiCr-F condition.

After 24 h at 800°C, a thin oxide scale (8 μm) formed on the TaTiCr-C alloy (Fig. 3(a)) and suffered from spallation in certain areas, suggesting poor adhesion to the substrate. The IRZ consists of fine, acicular precipitates within the bcc matrix near the surface and decorating Laves phase boundaries deeper into the specimen (65 μm). The Laves precipitates appear to remain unreacted near the surface, with the majority of reaction products located in the matrix. Compared to the TaTiCr-C condition, the TaTiCr-F condition developed a thinner oxide scale (4 μm) and a much shallower IRZ (20 μm) after testing (Fig. 3(b)), which is also consistent with the observed oxidation kinetics, Fig. 2. The precipitates in the IRZ were much finer and mostly segregated to Laves phase boundaries. The oxide scale also appeared to be more adherent, with fewer instances of spallation.

Table 2
Specific mass change (Δm), rate constant (k), and time exponent (n) for the TaTiCr-C and TaTiCr-F conditions after oxidation at all temperatures.

Temperature	Alloy	Δm after 24 h (mg/cm^2)	k (mg/cm^2·h^n)	n	Duration
800°C	TaTiCr-C	1.81	0.06	1.00	0–24 h
	TaTiCr-F	0.68	0.02	1.00	0–24 h
1000°C	TaTiCr-C	4.90	0.20	0.95	0–24 h
	TaTiCr-F	22.3	5.94	0.74	0–1 h
			3.27	0.48	1–24 h
1200°C	TaTiCr-C	7.23	1.87	0.34	0–24 h
	TaTiCr-F	25.2	1.73	0.83	0–24 h
1400°C	TaTiCr-C	26.0	2.88	0.37	0–2 h
			5.81	0.42	2–24 h
	TaTiCr-F	60.1	5.64	1.05	0–3 h
			7.72	0.48	3–24 h

After 24 h at 1000°C, a thicker (22 μm), porous oxide scale formed on the TaTiCr-C alloy. The scale appeared reasonably adherent, with no apparent spallation (Fig. 3(c)). Remnant prior Laves particles were observed within the inner portion of the scale, indicating internal oxidation during high temperature exposure. Within the IRZ, fine precipitates were found within the matrix just below the scale, transitioning into thicker, lenticular morphologies permeating deeper into the specimen, reaching a depth of 84 μm. The TaTiCr-F condition developed a much thicker scale after testing (75 μm), decorated with pores and containing many individual layers (Fig. 3(d)). Within the IRZ, the precipitates were slightly finer than in the TaTiCr-C condition and remained within the matrix, decorating Laves phase boundaries and penetrating 60 μm into the substrate.

After 24 h at 1200°C, the slightly thicker oxide scale (30 μm) was more dense and compact than at 1000°C, with distinct layers and good adherence (Fig. 3(e)). At the scale/IRZ interface, prior Laves precipitates transformed into a unique reaction product not observed at 1000°C and 800°C (determined to be Ta_2N from previous work [27]). The IRZ again contained dark precipitates, however they were consistently thicker and penetrated deeper into the specimen than at other temperatures (170 μm). The TaTiCr-F alloy formed a much thicker oxide scale (100 μm) consisting of three prominent regions with many pores separated by lateral cracks running parallel to the scale surface (Fig. 3(f)). The IRZ also penetrated far deeper (235 μm) and consisted of similar lenticular precipitates, again remaining localized to the matrix phase.

The thickest scale and deepest IRZ for both microstructural conditions were observed after 24 h at 1400°C. The TaTiCr-C condition displayed an oxide scale that was 97 μm thick and contained two prominent lateral cracks, separating the scale from the substrate (Fig. 3(g)). The IRZ was deeper than the other conditions, penetrating 750 μm into the specimen, indicating rapid oxidation as seen in the kinetic constants extracted from kinetic data (Table 2). Within the IRZ, significant microstructural decomposition occurred, comprised of thick, dark precipitates and additional precipitates within the prior Laves particles. The TaTiCr-F condition developed a very thick scale (200 μm) and deep IRZ (850 μm). The oxide scale contained five distinct regions with multiple layers and had lateral porosity and cracks separating each region (Fig. 3(h)). The IRZ was morphologically very similar to the TaTiCr-F condition. Previous studies on the TaTiCr-C condition revealed that these internal reaction products were complex nitrides, with Cr_3Ta_3N forming from the prior Laves precipitates and secondary $(Ta,Ti)_2N$ precipitates dispersed through the IRZ [27].

Comparing the outer oxide scale thickness and IRZ depth between the TaTiCr-C and TaTiCr-F conditions, the reactions were more severe for TaTiCr-F at all temperatures except for 800°C (Fig. 4). There is a notable increase in IRZ depth compared to scale thickness at 1400°C. This is most likely due to the fast diffusion in this temperature regime in addition to nitrogen permeability and internal nitridation, which has been discussed in previous work [27]. Mechanistic effects responsible for this change will be discussed in Section 3.4.

3.3.1. Reaction products after 24 h at 800°C

Composite SEM-EDS maps of the oxidized cross-sections after 24 h at 800°C are shown in Fig. 5 for the TaTiCr-C (Fig. 5(a)) and TaTiCr-F (Fig. 5(b)) conditions. Both oxide scales contain TiO_2, Cr_2O_3, mixed $(Cr,Ta,Ti)O_2$ oxides, and Ta_2O_5 (Table 3). Morphologically, the scales are similar, with an outer layer of TiO_2 above a prominent Cr_2O_3 layer mixed with $(Cr,Ta,Ti)O_2$ regions. A layer of Ta_2O_5 was also observed at the scale/IRZ interface. Within the IRZ, the unreacted Laves precipitates and bcc matrix are clearly discernable. The compositions of the fine, Ti-rich precipitates evident in BSE micrographs (Fig. 3(a),(b)) were not quantifiable through SEM-EDS due to their fine-scale morphology.

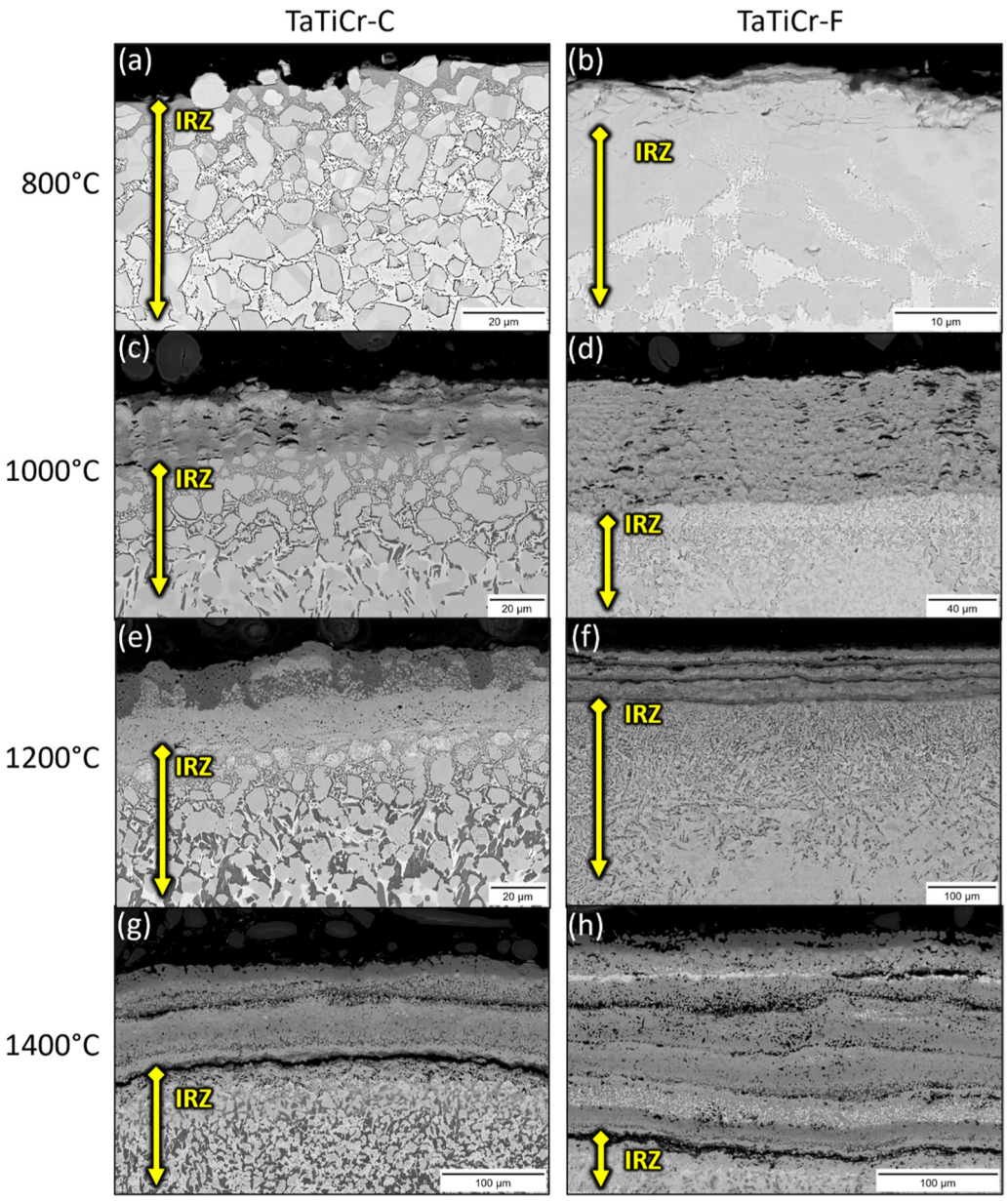

Fig. 3. BSE micrographs of oxide scale and IRZ cross-sections for TaTiCr-C (left) and TaTiCr-F (right) after 24 h exposure at (a,b) 800°C, (c,d) 1000°C, (e,f) 1200°C, (g,h) 1400°C. Note scale bar difference between conditions.

However, the previous study on the TaTiCr-C condition revealed using STEM-EDS that the precipitates were TiN. Additionally, the previous study showed that just below the scale exists a region of superfine lamellar TiN, most likely formed via discontinuous precipitation from the matrix [27]. It is reasonable to assume that the precipitates in TaTiCr-F are of similar character (i.e., TiN) as that of TaTiCr-C.

3.3.2. *Reaction products after 24 h at 1000°C*

At 1000°C and above, stark differences in oxide scale morphology were observed for the coarse and fine microstructural conditions. SEM-EDS composite maps after oxidation at 24 h at 1000°C for the TaTiCr-C and TaTiCr-F are shown in Fig. 6(a) and Fig. 6(b), respectively. Both oxide scales consisted of an outer layer of TiO_2 with an underlying layer of Cr_2O_3 (Table 4). Below these two oxide layers in the TaTiCr-C alloy, a layer of mixed (Cr,Ta,Ti)O_2 oxides formed (Fig. 6(a), Table 4). Deeper into the oxidized region, bands of Cr_2O_3 and mixed (Cr,Ta,Ti)O_2 oxides alternate progressing inward. It is worth noting that within the regions identified as (Cr,Ta,Ti)O_2, varied elemental enrichment can be observed with Cr, Ti and Ta, designated with bolded cations in labels, e.g., (Cr,**Ta, Ti**)O_2). Morphologically, the TaTiCr-F scale is much thicker (Fig. 6(b)) and contains many layers of repeating oxide structures. This is suggestive of repetitive, selective oxidation leading to the formation of an iterative oxide scaling morphology due to sequential depletion of oxidizing elements. This phenomenon has been observed in other RCCA systems (e.g., TaTiCr alloys [26], CrNbTaTi [25]) and is reported to be due to solute depletion that drives local chemistry changes and alters thermodynamically favored oxides. During the internal oxidation of TaTiCr, it is hypothesized that this effect occurs sequentially and results in the formation of repeating oxide layers. In the case of TaTiCr-F, the repeating oxide species below the initial oxide layer are most prominently: TiO_2, Cr_2O_3, mixed (Cr,Ta,Ti)O_2, and Ta_2O_5 (Table 4). Within the IRZ, both alloys contained unreacted Laves precipitates, with TiN precipitates (appearing as the dark precipitates in the BSE micrographs (Fig. 3(c-d), Table 4) within the Ta-rich bcc matrix.

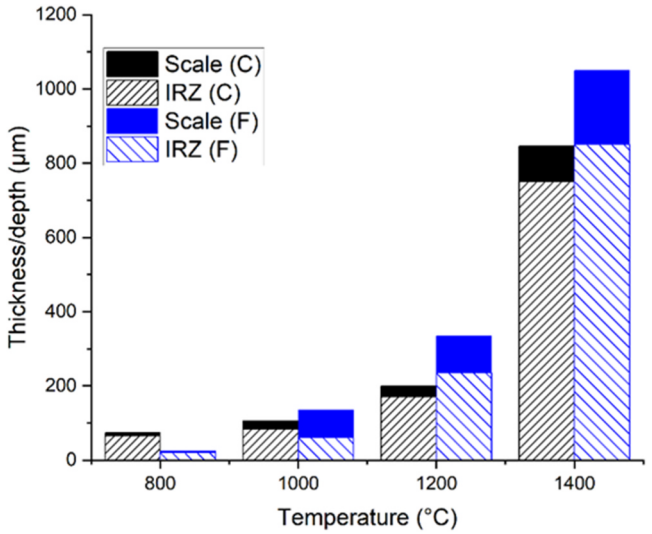

Fig. 4. Oxide scale thickness and IRZ depth of TaTiCr-C and TaTiCr-F alloys after 24 h of oxidation.

3.3.3. Reaction products after 24 h at 1200°C

After 24 h of exposure at 1200°C, both TaTiCr-C (Fig. 7(a)) and TaTiCr-F (Fig. 7(b)) formed oxide scales consisting of TiO_2, Cr_2O_3, and mixed oxides of the type $(Cr,Ta,Ti)O_2$ (Table 5). In a similar manner to the 1000°C condition, varied local enrichment of the $(Cr,Ta,Ti)O_2$ phase was observed. Some regions were richer in Cr and Ta, while others were richer in Ta and Ti, as evident by the variation in local coloring, most prominently observed in Fig. 7(b). Nevertheless, all of these mixed oxide phases are expected to form rutile structures with slightly varied lattice parameters [29]. Ta_2O_5 formation was not suppressed in the TaTiCr-F alloy and was evident in the repeating oxide scale layers, Fig. 7(b). Morphologically, the TaTiCr-C scale remained compact and highly adherent to the substrate, while the TaTiCr-F scale exhibited significant porosity/cracking throughout the scale, with a layered, repeating morphology similar to that observed in the 1000°C condition (Fig. 6(b)). Both scales formed a distinct, external, continuous "capping" layer of TiO_2. The repeating scale observed in the TaTiCr-F alloy contained discontinuous bands of Cr_2O_3 above layers of mixed $(Cr,Ta,Ti)O_2$ oxides, and Ta_2O_5. Within the IRZ, both alloys formed TiN, while the TaTiCr-C alloy also formed Ta_2N at the scale/IRZ interface (Table 5). The Ta_2N phase is also most likely present in the TaTiCr-F alloy, but it was not distinguishable at the resolution of SEM-EDS. The Laves phase that is present deeper into the IRZ appears to resist oxidation in a similar manner to the 1000°C (Fig. 6) and 800°C (Fig. 5) conditions.

3.3.4. Reaction products after 24 h at 1400°C

The reactions that occurred at 1400°C were the most severe in both microstructural conditions, with the most rapid oxidation kinetics (Table 2) and thickest oxide scales (Fig. 4). Both microstructural conditions displayed prominent scale layers; however, the TaTiCr-F condition (Fig. 8(b)) had two distinct repeating series of oxide layers, while the TaTiCr-C condition (Fig. 8(a)) had roughly four. Both oxide scales were complex, but most prominently contained TiO_2, Cr_2O_3, and mixed $(Cr,Ta,Ti)O_2$ oxides in a similar ordering sequence within the scale (Table 6). The TaTiCr-F condition had distinct layers of Ta_2O_5 as well, observed as a thin layer near the surface and a dispersed, speckled layer near the substrate (Table 6). While neither condition were observed to form continuous Cr_2O_3 after 24 h, continuous scales may have been present earlier in the oxidation process but not observed following complete exposure. The Cr_2O_3 layer morphology and porosity near the layers suggests that volatilization occurred during oxidation, which is especially evident in the TaTiCr-C kinetics containing two sub-parabolic regimes (Table 2).

3.4. Oxidation mechanisms of TaTiCr-C and TaTiCr-F conditions

Previous work in the TaTiCr system [26,27] has proposed that similar oxidation mechanisms observed in Ni-Cr-Al alloys [43–46] may play a role in the oxidation of RCCAs. In particular, Ni-Cr-Al alloys, with lower concentrations of Al, rely on the formation of external sluggish oxide layers (i.e., Cr_2O_3) to slow down the ingress of oxygen during the early stages of oxidation, thereby reducing the partial pressure of oxygen below the oxide scale and into the underlying alloy. This reduced oxygen availability minimizes the thermodynamic driving force for the formation of deleterious internal oxides like NiO, since it drives the formation of the most stable oxide species (e.g., Al_2O_3). This is highly advantageous since Al_2O_3 is highly protective when fully established (e.g. dense and compact), but generally forms slowly. This internal oxidation of Al_2O_3 eventually transitions to a continuous layer, thereby providing excellent oxidation resistance. Without the initial formation of Cr_2O_3 and/or $NiCr_2O_4$ at the surface (i.e. if only NiO formed), the chemical availability of oxygen deep into the alloy would remain relatively high and thereby induce strong competition in the formation of all possible oxides, which are not all protective. This limits oxidation resistance and

Table 3
SEM-EDS measurements for the observed phases in the TaTiCr-C and TaTiCr-F alloys after oxidation at 800°C for 24 h.

Phase	Alloy	Cr	Ta	Ti	O	N
TiO_2	TaTiCr-C	6.9	0.7	26.8	65.6	-
	TaTiCr-F	1.8	2.4	29.1	66.7	
Cr_2O_3	TaTiCr-C	30.4	9.5	3.4	61.5	-
	TaTiCr-F	22.1	9.5	5.7	63.2	-
$(Cr,Ta,Ti)O_2$	TaTiCr-C	15.5	12.1	6.4	66.1	-
	TaTiCr-F	8.8	11.9	12.2	67.2	-
Ta_2O_5	TaTiCr-C	-	-	-	-	-
	TaTiCr-F	2.4	22.4	5.2	70.0	-

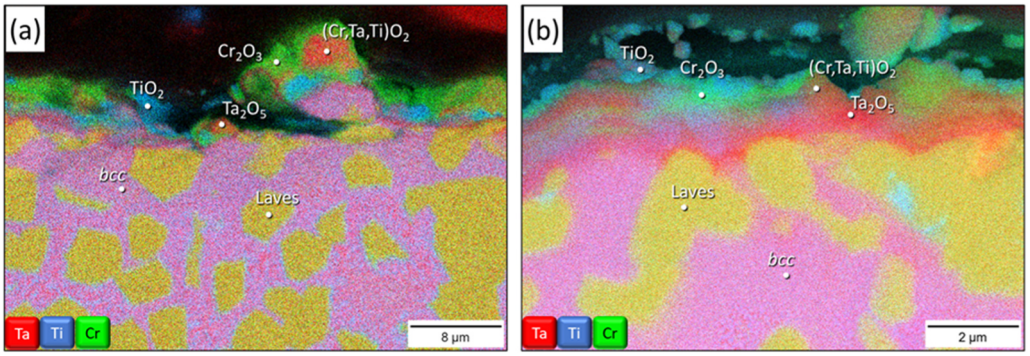

Fig. 5. Composite SEM-EDS maps of (a) TaTiCr-C and (b) TaTiCr-F after 24 h oxidation at 800°C. EDS maps are sub-regions of Figs. 3(a) and 3(b), respectively.

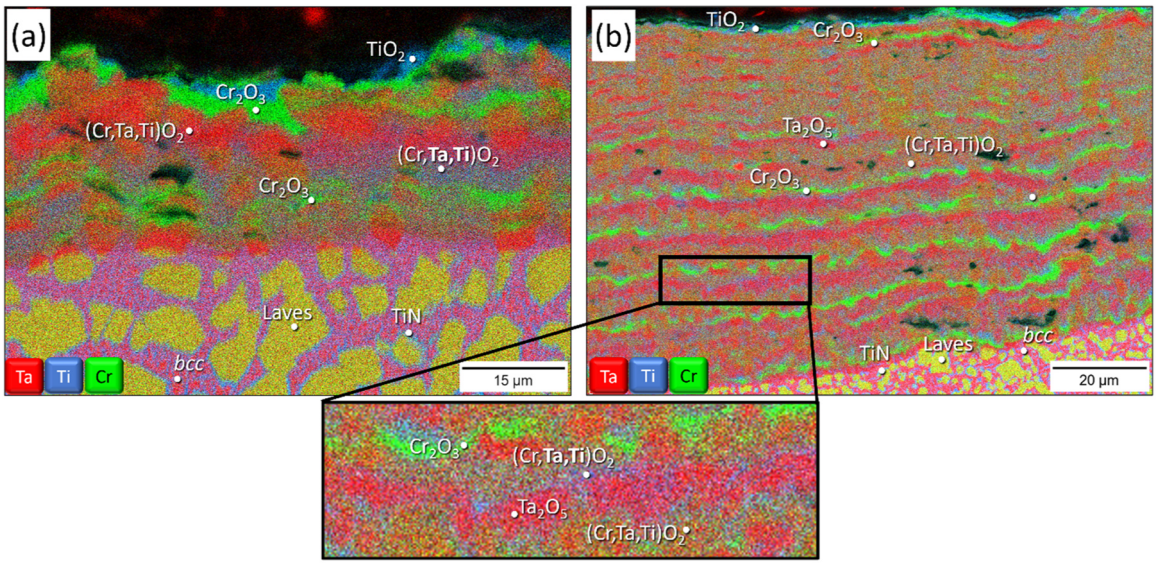

Fig. 6. Composite SEM-EDS maps of (a) TaTiCr-C and (b) TaTiCr-F after 24 h oxidation at 1000°C. EDS maps are sub-regions of Figs. 3(c) and 3(d), respectively.

Table 4
SEM-EDS measurements for the observed phases in the TaTiCr-C and TaTiCr-F alloys after oxidation at 1000°C for 24 h.

Phase	Alloy	Cr	Ta	Ti	O	N
TiO_2	TaTiCr-C	7.1	5.2	21.3	66.3	-
	TaTiCr-F	4.6	8.2	20.0	67.3	-
Cr_2O_3	TaTiCr-C	33.1	2.1	3.4	61.5	-
	TaTiCr-F	28.3	3.7	5.5	62.6	-
$(Cr,Ta,Ti)O_2$	TaTiCr-C	8.2	10.4	14.4	67.0	-
	TaTiCr-F	12.2	10.4	10.5	67.0	-
$(Cr,\mathbf{Ta,Ti})O_2$	TaTiCr-C	5.9	15.2	10.7	68.2	-
	TaTiCr-F	5.1	13.4	13.5	68.1	
Ta_2O_5	TaTiCr-C	-	-	-	-	-
	TaTiCr-F	2.4	22.4	5.2	70.0	-
TiN	TaTiCr-C	2.0	9.3	42.0	-	46.7
	TaTiCr-F	1.8	-	53.6	-	44.7

certainly hinders the formation of dense and continuous preferred oxide phases. This would also be observed in NiAl alloys with relatively low concentrations of Al.

For the TaTiCr system, the outer capping layer of TiO_2 and secondary formation of Cr_2O_3 are hypothesized to provide enough resistance to inward diffusing oxygen to promote the formation of more stable oxide species deeper in the alloy, as opposed to high fractions of Ta_2O_5, in this case. Again, the argument is that the chemical availability of oxygen below the external, continuous TiO_2 and Cr_2O_3 scales is minimized, thereby promoting the formation of the most stable oxides internally based on the local thermodynamics. As it turns out, the most stable oxides are generally more complex ($(Cr,Ta,Ti)O_2$) and will thus be thermodynamically preferred over simple deleterious oxides like Ta_2O_5 based on Gibbs free energy of formation when the chemical availability of oxygen is low [27]. The caveat to this proposed mechanism is that the protective layers (i.e., TiO_2 and Cr_2O_3) must be continuous in order to provide sufficient protection and to avoid deleterious oxide formation. In the case of the TaTiCr-C and TaTiCr-F, the Cr_2O_3 layer continuity is

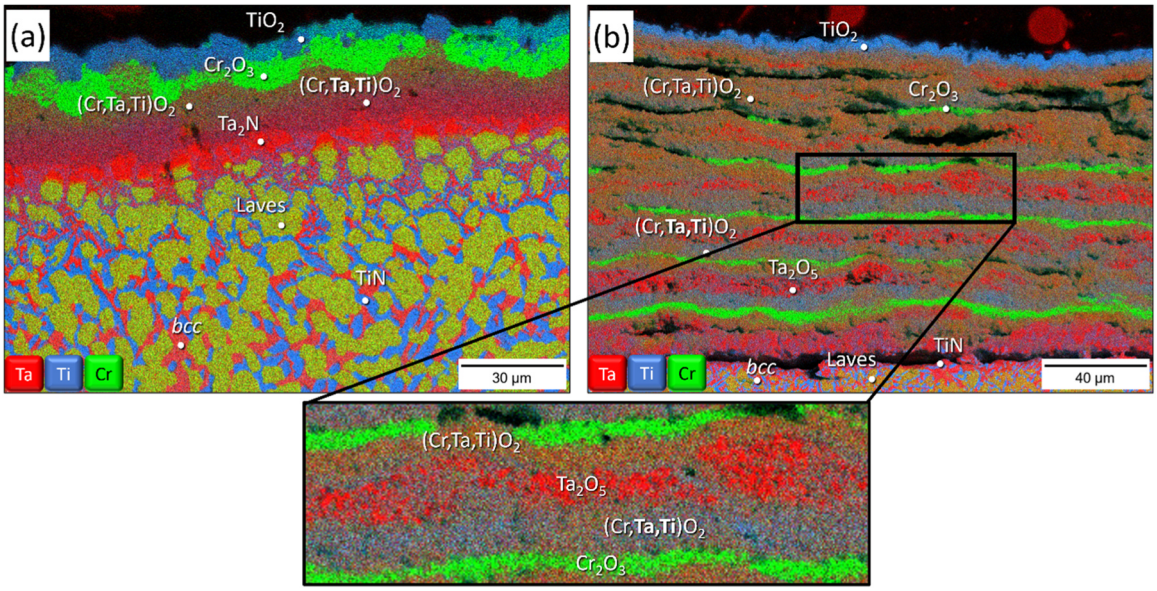

Fig. 7. Composite SEM-EDS maps of (a) TaTiCr-C and (b) TaTiCr-F after 24 h oxidation at 1200°C. EDS maps are sub-regions of Figs. 3(e) and 3(f), respectively.

Table 5
SEM-EDS measurements for the observed phases in the TaTiCr-C and TaTiCr-F alloys after oxidation at 1200°C for 24 h.

Phase	Alloy	Cr	Ta	Ti	O	N
TiO_2	TaTiCr-C	3.0	2.4	28.0	66.6	-
	TaTiCr-F	7.9	-	26.8	65.4	-
Cr_2O_3	TaTiCr-C	36.5	0.4	2.4	60.7	-
	TaTiCr-F	34.3	2.0	2.5	61.3	-
$(Cr,Ta,Ti)O_2$	TaTiCr-C	13.3	10.2	10.4	66.1	-
	TaTiCr-F	11.8	11.8	9.8	66.7	-
$(Cr,\mathbf{Ta,Ti})O_2$	TaTiCr-C	-	16.2	15.4	68.4	-
	TaTiCr-F	1.9	18.5	10.2	69.4	-
Ta_2O_5	TaTiCr-C	-	-	-	-	-
	TaTiCr-F	-	28.7	-	71.3	-
TiN	TaTiCr-C	0.2	8.6	46.8	1.0	43.4
	TaTiCr-F	-	3.0	44.2	-	52.8
Ta_2N	TaTiCr-C	1.0	67.8	6.6	1.3	23.4
	TaTiCr-F	-	-	-	-	-

not uniform between conditions, resulting in a drastic difference in oxidation behavior.

It is also hypothesized that the outer TiO_2 layer has an advantageous capping effect on the underlying Cr_2O_3 scale when it forms dense and continuously. At the high temperatures explored in this work, it is anticipated that Cr_2O_3 will volatilize to form CrO_3 gas. However, the outer TiO_2 scale appears to be advantageous in keeping the underlying Cr_2O_3 scale dense and compact, thereby promoting the favorable, local thermodynamics previously described above. A similar observation can be made from the work by Butler et al. [25] who showed that CrNb and CrNbTi had vast differences in Cr_2O_3 density after oxidation at 1200°C. In particular, the CrNb alloy formed a highly porous Cr_2O_3 oxide scale, while the CrNbTi alloy formed an outer TiO_2 capping layer and a dense underlying layer of Cr_2O_3. Similar observations on the advantageous role of external capping layers and Cr_2O_3 volatility have also been reported for Ni-base superalloys [47].

While the mixed $(Cr,Ta,Ti)O_2$ oxide has been reported to provide some degree of protection in related alloys [29], the observed morphology of this oxide in the TaTiCr-F alloy – in combination with discontinuous Cr_2O_3 layers – did not result in favorable oxidation resistance, as severe internal reactions containing the $(Cr,Ta,Ti)O_2$ oxide are seen at all temperatures above 800°C. $(Cr,Ta,Ti)O_2$ and the related complex oxide $CrTaO_4$ have been observed to preferentially form via internal oxidation modes in other systems [30]. While the presence of $(Cr,Ta,Ti)O_2$ can be indicative of oxidation resistance by neutralizing the presence of Ta_2O_5, this work and others [26,27] show that Cr_2O_3 formation also plays a significant role. In this manner, the most advantageous behavior occurs when the mixed complex oxides form in tandem with continuous protective oxides like Cr_2O_3.

To further explore this influence of Cr_2O_3, laves precipitate size and interparticle spacing are compared to Cr_2O_3 thickness after 24 h at 1200°C in Fig. 9. Similar data for CrNbTi and CrNbTaTi (after 8 h exposure at 1200°C) are shown for comparison [25]. These two additional alloys were included since they also form *bcc*+Laves microstructures. The relationship between precipitate diameter, interparticle spacing, and Cr_2O_3 layer thickness between these alloys shows a clear correlation, suggesting that Cr_2O_3 formation is heavily influenced by the Cr cations supplied by the Laves precipitates, and that smaller precipitates produce thinner, less dense Cr_2O_3 layers. Further, the Cr_2O_3 layer continuity scales directly with precipitate size, and thus, layer thickness.

While smaller precipitates/dispersoids have been shown to increase oxidation resistance in traditional alloys via accelerated outward

Table 6
SEM-EDS measurements for the observed phases in the TaTiCr-C and TaTiCr-F alloys after oxidation at 1400°C for 24 h.

Phase	Alloy	Cr	Ta	Ti	O	N
TiO_2	TaTiCr-C	3.2	3.3	26.8	66.7	-
	TaTiCr-F	2.0	2.1	29.2	66.7	-
Cr_2O_3	TaTiCr-C	37.3	1.0	1.1	60.6	-
	TaTiCr-F	38.5	0.5	0.8	60.3	-
$(Cr,Ta,Ti)O_2$	TaTiCr-C	11.2	11.5	10.6	66.7	-
	TaTiCr-F	10.7	11.6	10.4	67.3	-
$(Cr,\mathbf{Ta,Ti})O_2$	TaTiCr-C	2.2	16.1	12.7	69.0	-
	TaTiCr-F	1.9	17.4	11.5	69.2	-
Ta_2O_5	TaTiCr-C	-	-	-	-	-
	TaTiCr-F	-	25.7	-	74.3	-
TiN	TaTiCr-C	1.3	1.2	46.7	3.7	46.1
	TaTiCr-F	-	3.9	46.6	-	49.5

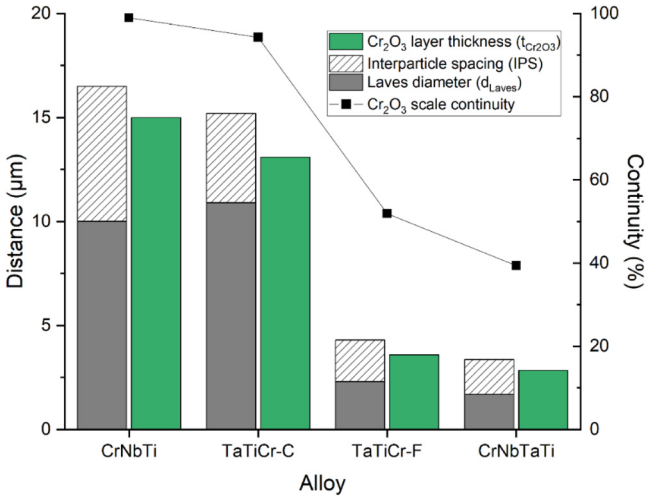

Fig. 9. Precipitate size and Cr_2O_3 layer thickness and continuity of TaTiCr-C and TaTiCr-F, compared to data from CrNbTi, and CrNbTaTi reported in [25].

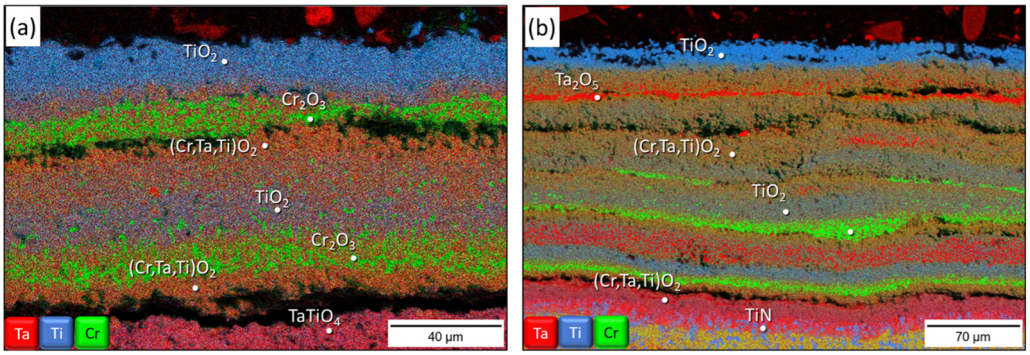

Fig. 8. Composite SEM-EDS maps of (a) TaTiCr-C and (b) TaTiCr-F after 24 h oxidation at 1400°C. EDS maps are sub-regions of Figs. 3(g) and 3(h), respectively.

diffusion of protective cations [39], the opposite effect was observed for the TaTiCr alloy in this work. Refining the microstructure to produce finer Laves particles that are spaced closer together produced an undesirable influence on the oxidation behavior. Fig. 10 illustrates the suggested chronology of oxide formation between the TaTiCr-C and TaTiCr-F conditions, in which (i) the initial external TiO_2 layer forms with small Cr_2O_3 islands on the Laves precipitates, as well as internal TiN needles and Ta_2O_5 formation. Secondarily (ii), the Cr_2O_3 layer coarsens and becomes continuous in the TaTiCr-C condition, reducing oxygen ingress further and slowing internal formation of Ta_2O_5. This ultimately results in subsequent reaction to form mixed $(Cr,Ta,Ti)O_2$ due to the local thermodynamics and reduced availability of oxygen. However, in the TaTiCr-F condition, the Cr_2O_3 layer is unable to coalesce and become fully continuous (or dense enough to provide reasonable protection) due to the higher fraction of Ta_2O_5 formed primarily in the matrix phase. For TaTiCr-C, the final stage (iii) results in further growth and substrate protection, with the three distinct layers observed in Fig. 7 (a), while the TaTiCr-F condition ends with sequential internal oxidation events and repeating oxide morphologies, due to the fineness and distribution of Laves particles, Fig. 7(b). The mechanisms suggested in this work share similarities to the mechanisms of TaMoCrTiAl alloys proposed by Schellert, et al. [48] in which initial discontinuous precipitates of Al_2O_3 and Cr_2O_3 observed in Ta-lean alloys $(Ta_{0–10}(MoCrTiAl)_{100–90})$ do not provide adequate protection from internal mixed complex oxide formation, resulting in a thicker internal oxide scale, whereas near equiatomic alloys $(Ta_{15–20}(MoCrTiAl)_{85–80})$ form nearly continuous layers of Cr_2O_3 and Al_2O_3 and resist severe internal oxidation, forming primarily $CrTaO_4/(Cr,Ta,Ti)O_2$.

The alloys explored in this work have been observed to suffer greatly from local solute changes (less pronounced in the TaTiCr-C condition), readily shifting the local thermodynamically favorable oxides to that of the enriched solute, thus resulting in the repetitive scales observed in the TaTiCr-F condition. It was also observed that microstructural refinement had a deleterious influence on oxidation mechanism. For the latter, one proposed mechanism is that instead of initiating external Cr_2O_3 formation, the additional phase boundaries in the refined microstructures accelerated the inward diffusion of oxygen, thereby maximizing the extent of internal oxidation and increasing the amount of internal Ta_2O_5 formation (as corroborated by the faster oxidation kinetics in the TaTiCr-F condition (Fig. 2, Table 3)). Additionally, the finer Cr reservoirs in the TaTiCr-F condition appear to be insufficient to promote the establishment of dense, continuous Cr_2O_3 scales to prevent enhanced internal oxidation, compared to the coarse Laves particles in the TaTiCr-C condition. This is also confounded with the abundant presence of internal Ta_2O_5 in the TaTiCr-F condition (Figs. 6(b),7(b),8(b)) also suggesting an unfavorable oxidation state, likely driven by the high availability of oxygen throughout the scale.

The two opposing oxidation behaviors is a complex phenomenon, ultimately deriving from the precipitate morphology and distribution differences between the two tested microstructural conditions. Finer dispersoids result in thinner, less continuous layers of Cr_2O_3, as well as accelerated internal diffusion of oxygen, resulting in the formation of a high degree of Ta_2O_5. On the contrary, the coarser precipitates form a dense, thick Cr_2O_3 layer to protect the substrate and provide excellent oxidation resistance in tandem with underlying $(Cr,Ta,Ti)O_2$ formation.

The results of this work demonstrate the importance that microstructure plays on the resulting oxidation mechanisms in RCCAs. Therefore, microstructure cannot and should not be neglected when exploring the active oxidation mechanisms in RCCAs.

4. Conclusions

This work reports the oxidation behaviors of a TaTiCr alloy with coarse (TaTiCr-C) and fine (TaTiCr-F) Laves precipitates. All conditions were tested for 24 h at 800°C, 1000°C, 1200°C, and 1400°C. The following key points can be made:

- The oxidation of the TaTiCr-C alloy resulted in far less mass gain and thinner oxide scales/shallower internal reaction zones (IRZs) compared to TaTiCr-F (except at 800°C), though, the reaction products were similar in all cases, consisting primarily of TiO_2, Cr_2O_3, and mixed $(Cr,Ta,Ti)O_2$ oxides.
- Microstructure morphology correlations were observed related to Cr_2O_3 scale thickness and continuity, suggesting that the Cr_2O_3 formation is highly dependent on Laves particle size and that coarser precipitates form thicker, more continuous Cr_2O_3 layers.
- Cr_2O_3 layer continuity and thickness is a major contributor to oxidation resistance, especially when formed in concert with complex refractory oxides like $(Cr,Ta,Ti)O_2$. It was found that a loss of continuity in the Cr_2O_3 scales (as observed in the TaTiCr-F alloy) resulted in poor oxidation performance, consisting of extensive internal oxidation and the formation of excess Ta_2O_5 and iterative, internal oxide layers. Additionally, it is hypothesized that continuous external Cr_2O_3 formation reduces underlying oxygen availability, thereby thermodynamically promoting the formation of more favorable internal complex oxides (with higher stability) compared to deleterious oxides (e.g. Ta_2O_5).
- Microstructure must be considered when evaluating oxidation performance in RCCAs, as vast differences in behavior can be observed between microstructural conditions with similar compositions.

CRediT authorship contribution statement

Peter C. Collins: Writing – review & editing, Supervision, Project

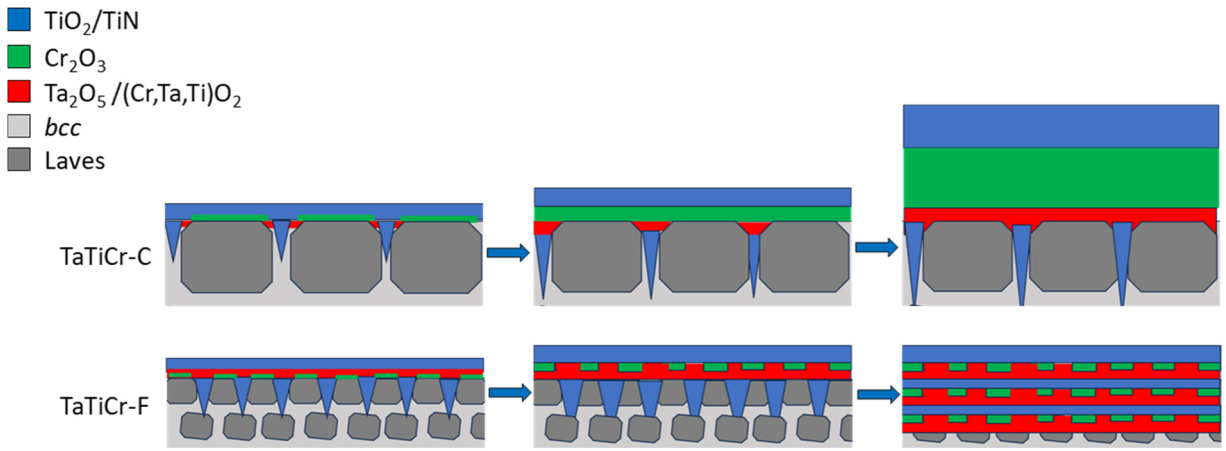

Fig. 10. Schematic of oxidation modes at 1200°C in the TaTiCr-C and TaTiCr-F conditions.

administration, Funding acquisition, Conceptualization. **Noah James Welch:** Writing – review & editing, Writing – original draft, Visualization, Methodology, Investigation, Formal analysis, Data curation, Conceptualization. **Maria J. Quintana:** Writing – review & editing, Methodology, Data curation, Conceptualization. **Todd M. Butler:** Writing – review & editing, Supervision, Methodology, Investigation, Conceptualization.

Declaration of Competing Interest

The authors declare that they have no known competing financial interests or personal relationships that could have appeared to influence the work reported in this paper.

Data availability

Data will be made available on request.

Acknowledgements

The authors acknowledge the support of the Center for Advanced Non-Ferrous Structural Alloys (CANFSA), an NSF Industry/University Cooperative Research Center (I/UCRC) between Iowa State University and The Colorado School of Mines under NSF-IIP award #1624748. The views, opinions and/or findings expressed are those of the author and should not be interpreted as representing the official views or policies of the Department of Defense or the U.S. Government.

References

[1] O.N. Senkov, S. Gorsse, D.B. Miracle, High temperature strength of refractory complex concentrated alloys, Acta Mater. 175 (2019) 394–405, https://doi.org/10.1016/j.actamat.2019.06.032.
[2] S. Sheikh, M.K. Bijaksana, A. Motallebzadeh, S. Shafeie, A. Lozinko, L. Gan, T.-K. Tsao, U. Klement, D. Canadinc, H. Murakami, S. Guo, Accelerated oxidation in ductile refractory high-entropy alloys, Intermetallics 97 (2018) 58–66, https://doi.org/10.1016/j.intermet.2018.04.001.
[3] J.R. DiStefano, B.A. Pint, J.H. DeVan, Oxidation of refractory metals in air and low pressure oxygen gas, Int J. Refract Met. Hard Mater. 18 (2000) 237–243, https://doi.org/10.1016/S0263-4368(00)00026-3.
[4] E. Pink, R. Eck, Refractory metals and their alloys. in: Materials Science and Technology, Wiley-VCH Verlag GmbH & Co. KGaA, Weinheim, Germany, 2006, https://doi.org/10.1002/9783527603978.mst0088.
[5] O. Kubaschewski, B.E. Hopkins, Oxidation mechanisms of niobium, tantalum, molybdenum and tungsten, J. Less Common Met. 2 (1960) 172–180, https://doi.org/10.1016/0022-5088(60)90012-6.
[6] G.T.J. Mayo, W.H. Shepherd, A.G. Thomas, Oxidation behaviour of niobium-chromium alloys, J. Less Common Met. 2 (1960) 223–232, https://doi.org/10.1016/0022-5088(60)90016-3.
[7] T. Maruyama, K. Yanagihara, High temperature oxidation and pesting of Mo(Si,Al) 2, Mater. Sci. Eng.: A 239–240 (1997) 828–841, https://doi.org/10.1016/S0921-5093(97)00673-4.
[8] R. Smith, The development of oxidation-resistant niobium alloys, J. Less Common Met. 2 (1960) 191–206, https://doi.org/10.1016/0022-5088(60)90014-X.
[9] H.J. Grabke, G.H. Meier, Accelerated oxidation, internal oxidation, intergranular oxidation, and pesting of intermetallic compounds, Oxid. Met. 44 (1995) 147–176, https://doi.org/10.1007/BF01046726.
[10] G. Mehboob, M.-J. Liu, T. Xu, S. Hussain, G. Mehboob, A. Tahir, A review on failure mechanism of thermal barrier coatings and strategies to extend their lifetime, Ceram. Int 46 (2020) 8497–8521, https://doi.org/10.1016/j.ceramint.2019.12.200.
[11] O.N. Senkov, G.B. Wilks, J.M. Scott, D.B. Miracle, Mechanical properties of Nb25Mo25Ta 25W25 and V20Nb20Mo 20Ta20W20 refractory high entropy alloys, Intermetallics 19 (2011) 698–706, https://doi.org/10.1016/j.intermet.2011.01.004.
[12] T.M. Butler, O.N. Senkov, M.A. Velez, T.I. Daboiku, Microstructures and mechanical properties of CrNb, CrNbTi, and CrNbTaTi concentrated refractory alloys, Intermetallics 138 (2021), https://doi.org/10.1016/j.intermet.2021.107323.
[13] V. Soni, O.N. Senkov, B. Gwalani, D.B. Miracle, R. Banerjee, Microstructural design for improving ductility of an initially brittle refractory high entropy alloy, Sci. Rep. 8 (2018), https://doi.org/10.1038/s41598-018-27144-3.
[14] B. Gorr, F. Müller, M. Azim, H.-J. Christ, T. Müller, H. Chen, A. Kauffmann, M. Heilmaier, High-temperature oxidation behavior of refractory high-entropy alloys: effect of alloy composition, Oxid. Met. 88 (2017) 339–349, https://doi.org/10.1007/s11085-016-9696-y.
[15] T.M. Butler, K.J. Chaput, J.R. Dietrich, O.N. Senkov, High temperature oxidation behaviors of equimolar NbTiZrV and NbTiZrCr refractory complex concentrated alloys (RCCAs), J. Alloy. Compd. 729 (2017) 1004–1019, https://doi.org/10.1016/j.jallcom.2017.09.164.
[16] S. Schellert, B. Gorr, S. Laube, A. Kauffmann, M. Heilmaier, H.J. Christ, Oxidation mechanism of refractory high entropy alloys Ta-Mo-Cr-Ti-Al with varying Ta content, Corros. Sci. 192 (2021), https://doi.org/10.1016/j.corsci.2021.109861.
[17] O.N. Senkov, T.I. Daboiku, T.M. Butler, M.S. Titus, N.R. Philips, E.J. Payton, High-temperature mechanical properties and oxidation behavior of Hf-27Ta and Hf-21Ta-21X (X is Nb, Mo or W) alloys, Int J. Refract Met. Hard Mater. 96 (2021) 105467, https://doi.org/10.1016/j.ijrmhm.2020.105467.
[18] O.N. Senkov, G.B. Wilks, D.B. Miracle, C.P. Chuang, P.K. Liaw, Refractory high-entropy alloys, Intermetallics 18 (2010) 1758–1765, https://doi.org/10.1016/j.intermet.2010.05.014.
[19] N.R. Philips, M. Carl, N.J. Cunningham, New opportunities in refractory alloys, Metall. Mater. Trans. A 51 (2020) 3299–3310, https://doi.org/10.1007/s11661-020-05803-3.
[20] O.N. Senkov, S.V. Senkova, D.M. Dimiduk, C. Woodward, D.B. Miracle, Oxidation behavior of a refractory NbCrMo0.5Ta0.5TiZr alloy, J. Mater. Sci. 47 (2012) 6522–6534, https://doi.org/10.1007/s10853-012-6582-0.
[21] O.N. Senkov, C.F. Woodward, Microstructure and properties of a refractory NbCrMo0.5Ta0.5TiZr alloy, Mater. Sci. Eng. A 529 (2011) 311–320, https://doi.org/10.1016/j.msea.2011.09.033.
[22] F. Müller, B. Gorr, H.-J. Christ, J. Müller, B. Butz, H. Chen, A. Kauffmann, M. Heilmaier, On the oxidation mechanism of refractory high entropy alloys, Corros. Sci. 159 (2019) 108161, https://doi.org/10.1016/j.corsci.2019.108161.
[23] O.N. Senkov, D.B. Miracle, K.J. Chaput, J.-P. Couzinie, Development and exploration of refractory high entropy alloys—A review, J. Mater. Res. 33 (2018) 3092–3128, https://doi.org/10.1557/jmr.2018.153.
[24] T.M. Butler, K.J. Chaput, Native oxidation resistance of Al20Nb30Ta10Ti30Zr10 refractory complex concentrated alloy (RCCA), J. Alloy. Compd. 787 (2019) 606–617, https://doi.org/10.1016/j.jallcom.2019.02.128.
[25] T.M. Butler, O.N. Senkov, T.I. Daboiku, M.A. Velez, H.E. Schroader, L.G. Ware, M. S. Titus, Oxidation behaviors of CrNb, CrNbTi, and CrNbTaTi concentrated refractory alloys, Intermetallics 140 (2022), https://doi.org/10.1016/j.intermet.2021.107374.
[26] N.J. Welch, M.J. Quintana, T.M. Butler, P.C. Collins, High-temperature oxidation behavior of TaTiCr, Ta4Ti3Cr, Ta2TiCr, and Ta4TiCr3 concentrated refractory alloys, J. Alloy. Compd. 941 (2023) 169000, https://doi.org/10.1016/j.jallcom.2023.169000.
[27] N.J. Welch, M.J. Quintana, S.J. Kuhr, T.M. Butler, P.C. Collins, Intermediate and high-temperature oxidation behavior of an equiatomic TaTiCr RCCA from 800 °C to 1400 °C, Int J. Refract Met. Hard Mater. (2023) 106437, https://doi.org/10.1016/j.ijrmhm.2023.106437.
[28] B. Gorr, F. Müller, S. Schellert, H.-J. Christ, H. Chen, A. Kauffmann, M. Heilmaier, A new strategy to intrinsically protect refractory metal based alloys at ultra high temperatures, Corros. Sci. 166 (2020) 108475, https://doi.org/10.1016/j.corsci.2020.108475.
[29] S. Schellert, M. Weber, H.J. Christ, C. Wiktor, B. Butz, M.C. Galetz, S. Laube, A. Kauffmann, M. Heilmaier, B. Gorr, Formation of rutile (Cr,Ta,Ti)O2 oxides during oxidation of refractory high entropy alloys in Ta-Mo-Cr-Ti-Al system, Corros. Sci. 211 (2023) 110885, https://doi.org/10.1016/j.corsci.2022.110885.
[30] S. Schellert, B. Gorr, H. Christ, C. Pritzel, S. Laube, A. Kauffmann, M. Heilmaier, The effect of Al on the formation of a CrTaO4 layer in refractory high entropy alloys Ta-Mo-Cr-Ti-xAl, Oxid. Met. 96 (2021), https://doi.org/10.1007/s11085-021-10046-7.
[31] B. Gorr, S. Schellert, F. Müller, H.-J. Christ, A. Kauffmann, M. Heilmaier, Current status of research on the oxidation behavior of refractory high entropy alloys, Adv. Eng. Mater. 23 (2021) 2001047, https://doi.org/10.1002/adem.202001047.
[32] C. Leyens, M. Peters, W.A. Kaysser, Influence of microstructure on oxidation behaviour of near-α titanium alloys, Mater. Sci. Technol. 12 (1996) 213–218, https://doi.org/10.1179/mst.1996.12.3.213.
[33] A. Gil, H. Hoven, E. Wallura, W.J. Quadakkers, 1993The Effect of Microstructure on the Oxidation Behaviour of Tiai-based Intermetallics..
[34] S.K. Samanta, S.K. Mitra, T.K. Pal, Effect of rare earth elements on microstructure and oxidation behaviour in TIG weldments of AISI 316L stainless steel, Mater. Sci. Eng.: A 430 (2006) 242–247, https://doi.org/10.1016/j.msea.2006.05.063.
[35] A. Casadebaigt, J. Hugues, D. Monceau, Influence of microstructure and surface roughness on oxidation kinetics at 500–600 °C of Ti–6Al–4V alloy fabricated by additive manufacturing, Oxid. Met. 90 (2018) 633–648, https://doi.org/10.1007/s11085-018-9859-0.
[36] X. Wang, J.A. Szpunar, Effects of grain sizes on the oxidation behavior of Ni-based alloy 230 and N, J. Alloy. Compd. 752 (2018) 40–52, https://doi.org/10.1016/j.jallcom.2018.04.173.
[37] L. Liu, Z. Yang, C. Zhang, M. Ueda, K. Kawamura, T. Maruyama, Effect of grain size on the oxidation of Fe–13Cr–5Ni alloy at 973K in Ar–21vol%O2, Corros. Sci. 91 (2015) 195–202, https://doi.org/10.1016/j.corsci.2014.11.020.
[38] H.Z. Zheng, S.Q. Lu, Y. Huang, Influence of grain size on the oxidation behavior of NbCr2 alloys at 950–1200°C, Corros. Sci. 51 (2009) 434–438, https://doi.org/10.1016/j.corsci.2008.11.014.
[39] W.J. Quadakkers, K. Bongartz, The prediction of breakaway oxidation for alumina forming ODS alloys using oxidation diagrams, Mater. Corros. /Werkst. Und Korros. 45 (1994) 232–241, https://doi.org/10.1002/maco.19940450404.
[40] T.M. Butler, M.J. Pavel, M.L. Weaver, The effect of annealing on the microstructures and oxidation behaviors of AlCoCrFeNi complex concentrated

alloys, J. Alloy. Compd. 956 (2023) 170391, https://doi.org/10.1016/j.jallcom.2023.170391.
[41] M.J. Pavel, M.L. Weaver, Microstructural impacts on the oxidation of multi-principal element alloys, High. Temp. Corros. Mater. (2024), https://doi.org/10.1007/s11085-024-10225-2.
[42] H.Z. Zheng, S.Q. Lu, Y. Huang, Influence of grain size on the oxidation behavior of NbCr2 alloys at 950–1200°C, Corros. Sci. 51 (2009) 434–438, https://doi.org/10.1016/j.corsci.2008.11.014.
[43] S. Han, D.J. Young, Oxidation - Nitridation of Ni-Cr-Al alloys, Mater. Res. 7 (2004) 11–16, https://doi.org/10.1590/S1516-14392004000100003.
[44] C.S. Giggins, F.S. Pettit, Oxidation of Ni-Cr-Al alloys between 1000° and 1200°C, J. Electrochem Soc. 118 (1971) 1782, https://doi.org/10.1149/1.2407837.
[45] I.A. Kvernes, P. Kofstad, The oxidation behavior of some Ni-Cr-Al alloys at high temperatures, Metall. Trans. 3 (1972) 1511–1519, https://doi.org/10.1007/BF02643040.
[46] F.H. Stott, G.C. Wood, M.G. Hobby, A comparison of the oxidation behavior of Fe-Cr-Al, Ni-Cr-Al, and Co-Cr-Al alloys, Oxid. Met. 3 (1971) 103–113, https://doi.org/10.1007/BF00603481.
[47] T. Sand, C. Geers, Y. Cao, J.E. Svensson, L.G. Johansson, Effective reduction of chromium-oxy-hydroxide evaporation from Ni-base Alloy 690, Oxid. Met. 92 (2019) 259–279, https://doi.org/10.1007/s11085-019-09935-9.
[48] S. Schellert, B. Gorr, S. Laube, A. Kauffmann, M. Heilmaier, H.J. Christ, Oxidation mechanism of refractory high entropy alloys Ta-Mo-Cr-Ti-Al with varying Ta content, Corros. Sci. 192 (2021) 109861, https://doi.org/10.1016/j.corsci.2021.109861.